

Topography and the shallow slip deficit inference

T. Ben Thompson^{1,*} Brendan J. Meade¹

¹Department of Earth and Planetary Science, Harvard University,
Cambridge, MA, USA
April 13, 2018

1 Abstract

Images of earthquake slip serve as the foundation for understanding the distribution of coseismic energy release, theories about rupture propagation, and fault mechanics. Geodetic slip images are inferred using elastic models that link surface observations to fault activity at depth. To date, almost all elastic models used for these common calculations [10, 14, 19, 23] include the assumption that the Earth is flat [1, 6, 11], even for earthquakes in regions of extreme topographic relief like the 2008 $M_W = 7.9$ Wenchuan earthquake at the Longmenshan range-front. Here we develop three-dimensional boundary element models that explicitly include topographic relief and find that the classical flat Earth assumption may induce errors $> 100\%$ in imaged coseismic slip. This topographic effect is important even in regions with small topographic gradients (1-5% , 1992 $M_W = 7.3$ Landers) and can lead to the inaccurate inference of a shallow slip deficit [9]. These results illustrate that understanding earthquake behaviors will require more accurate models not only in terms of physical processes but also in terms of geologic fidelity.

2 Introduction

Coseismic fault slip is a primary mechanism allowing the horizontal motions of tectonic plates and the growth of topographic relief at plate boundaries. Mapping the spatial distribution of coseismic slip and interpreting these images in the context of tectonic evolution, thermo-mechanical rock properties, and earthquake dynamics, has become a fundamental tool in earthquake science. However, the physical models used to infer coseismic slip distributions tend to be simplified in several respects (e.g., planar fault surfaces, homogeneous material properties, half space approximation). Here we demonstrate that neglecting topographic relief in the half-space approximation leads to large errors in the inference of coseismic slip distributions especially in continental regions. The effects of topography have been studied on subduction zone settings ([6, 12], however topographic effects are far larger for continental earthquakes where GPS stations are distributed near the earthquake hypocenter and across significant topographic relief.

The effect of local surface topography on coseismic slip distributions bears particularly on the discussion of a potential shallow slip deficit. Geodetic slip estimates for several major continental earthquakes suggest significantly lower coseismic slip magnitudes at the shallowest depths [9, 24]. Several attempts to reconcile this putative shallow slip deficit with the general observation that geodetic and geologic slip rate estimate tend to agree [15, 21] have included rapid shallow creep between large earthquakes, afterslip [9], and a lack of near-field observations [24]. Here, we demonstrate that the reported inference of a shallow slip deficit may be an error caused by the use of a flat earth model rather than a model that explicitly represent topography in the vicinity of large continental earthquakes.

The absence of topography in most physical models of quasistatic earthquake slip is largely due to computational convenience. The most common static model of an earthquake is that of a fault embedded in an infinite half-space. Because the atmosphere applies a negligible stress on the Earth’s surface, a zero traction boundary condition is assumed for the surface of the half-space. Given these assumptions, [1] analytically solved the forward modelling problem of computing the displacement at the surface of the half-space caused by slip on the fault. Then, for inverse problems, the slip on the fault is inferred from observed displacements at the surface of the half-space.

In reality, the location of the traction free surface boundary condition is determined by the local topography. A large topographic gradient will create a non-Andersonian stress state at the surface that will influence both forward and inverse models. Previous slip inversions including topography have primarily studied subduction zones [6, 12]. The low topographic gradient in a megathrust environment and the large distance between the fault, the displacement observations and the topography leads to a small topographic effect. In contrast, for the continental earthquakes we study, steep topographic gradients are found both near the fault and near the observations.

Here we explicitly model the local topography and large-scale curvature of the Earth using a three-dimensional elastic Galerkin boundary element method (BEM) [4]. This approach enables analyzing models including 3D topography, complex fault geometry, spatially variable fault slip, material property contrasts and time-dependent slip. We are able to solve large scale problems with this approach through two innovations: 1) a new lookup-table-based numerical integration methodology for fast and accurate computation of nearfield Green’s function element interaction integrals and 2) farfield element interactions are computed using a GPU-accelerated implementation of the dual tree traversal fast multipole method [8, 22].

3 Implications of topography for geodetic slip inversion

We first analyze a simplified model of a fault beneath a mountain to isolate the effects of topography on slip inversion. A 70 km long fault is buried from 3 to 15 km depth and a Gaussian-shaped hill is centered over the middle of the fault – see Figure 1a for a cross-sectional view. We run a forward model with 3.5 meters of slip (similar to the average slip during the Landers earthquake) on the entire fault surface to obtain surface displacements everywhere on the free surface. These surface displacements are then inverted using both a model including topography (Figure 1b) and a model with a flat free surface (Figure 1c). The difference in inferred slip between the model with topography and the model without topography is a quantitative measure of the error incurred by using half-space models.

The inversion step is done using standard least squares methods with L2-

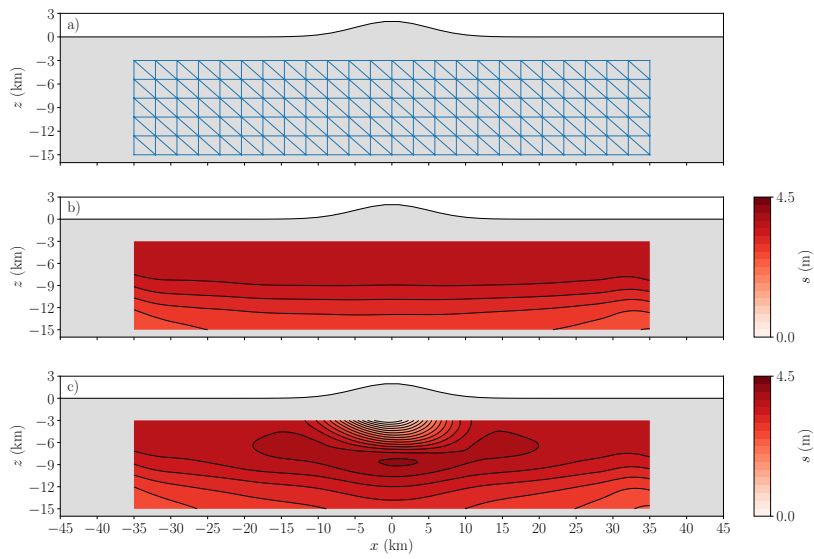


Figure 1: a) A fault model and topographic profile shown in cross section for testing the effects of topography on geodetic slip inversion. b) The slip distribution inferred when the "correct" topographic model is used. c) The slip distribution inferred when the "incorrect" flat half-space model is used.

norm regularization on the slip vector. The regularization parameter is chosen so that the total moment for the inferred slip distribution matches the total moment of the input slip distribution. Due to regularization effects, the original slip distribution is not perfectly recovered by inverting the model including topography (Figure 1b). However, the slip distribution is uniform along strike and within 10% of uniform with depth. Thus, the inversion process is recovering a good approximation of the correct slip distribution.

In comparison, inverting without topography shows a large slip deficit underneath the high topography with the highest slip deficit underneath the highest topography. In contrast with the uniform input slip distribution, this slip deficit shows that neglecting topographic effects incurs locally large errors in the near surface and underneath high and/or steep topography. Underneath the highest topography, the error reaches 100%.

The topographic effects we have demonstrated can be separated into two primary parts. First, there is the effect due to the shift in the position of the free surface (zero traction) boundary condition. This modifies the full displacement field and can be thought of as a “global” phenomenon. Second, there is the effect of moving the location of an observation point. Including or ignoring the presence of a mountain will result in a change in the distance from the observation site to the fault. While this effect is local in that it only influences single observations, it can have a large influence, particularly if the observation site is in the nearfield. In the case of this simplified hill-over-fault model, 80% of the effect comes from modifying the position of the free surface, and the remaining 20% comes from the source-to-observation distance effect.

4 Topographic effects and the prevalence of shallow slip for the Landers and Wenchuan earthquakes

We study how these topographic effects influence the inferred slip distribution in both the 2008 M_W 7.9 Wenchuan earthquake and the M_W 7.3 Landers earthquake.

For this study, the Wenchuan earthquake is especially interesting because it occurred in one of steepest regions on Earth. The Longmenshan mountain range rises 5 km from the Sichuan Basin to the Tibetan Plateau across a distance of less than 30 km. Using our insights from the synthetic example in the previous section, we expect this topographic signature to influence the inferred slip distribution due to both the 15% regional topographic gradient and the 5 km difference in baseline topography between the Sichuan Basin and the Tibetan Plateau.

During the Wenchuan earthquake, the Beichuan and Pengguan faults exhibited a mix of thrust and right-lateral sense slip for 250 km along strike with an average offset of 5-7 meters [14, 16]. The rupture devastated the region, leading to approximately 70,000 fatalities [25].

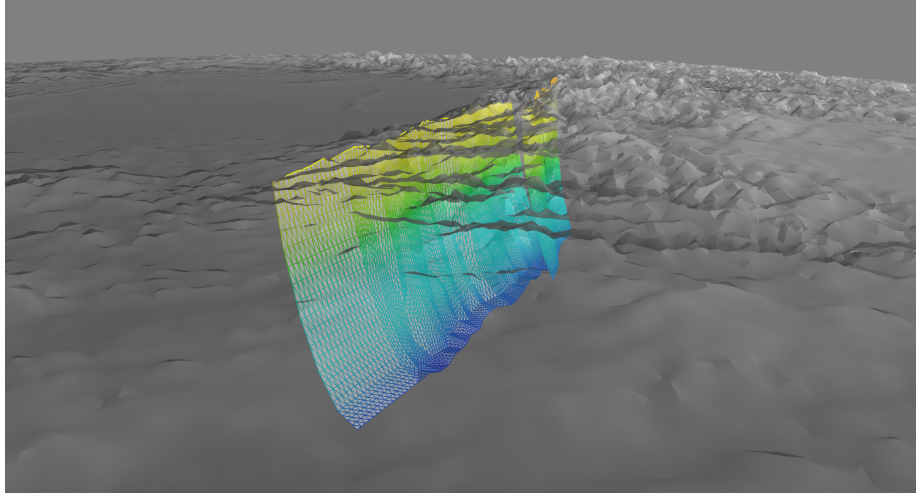


Figure 2: A view of the Wenchuan model looking south from high above the Earth’s surface at the fault model through transparent mountainous topography. The fault is color-coded according to depth, with the deepest parts of the fault approximately 22 km beneath the surface. The low, flat Sichuan basin is visible on the left, separated from the high, flat Tibetan Plateau on the right by the Longmenshan range in the center above the fault. The curvature of the Earth is visible in the background.

We construct a data-derived geometric model of the Wenchuan earthquake including topography and earth curvature. The geometry of the Beichuan Fault and Pengguan faults has been inferred from structural interpretations and seismic observations [17]. The surface topography is derived from the Shuttle Radar Topography Mission [26]. The topographic and fault models are realized in the WGS-84 spheroid (Figure 2). The mesh length scale used for the topography varies from 2 km to 4 km depending on the distance to the fault, with a total of 379,872 elements.

We invert GPS data and triangulation data [18], containing a total of 506 displacement observations. We use the same Tikhonov-regularized least squares approach as in the synthetic example. The inferred slip distribution we obtain (Figure 3) is broadly similar to previous slip distributions [14, 16, 18] with a transition from primarily dip-slip in the southwest to primarily right-lateral strike-slip in the northeast. However, the distribution of slip with depth is skewed even more towards a shallow-slip-dominant earthquake than previous analyses. We find 50% of coseismic moment release occurring above 9 km depth (Figure 3), compared with 50% of moment above 11 km in a previous slip distribution [20].

The Landers earthquake occurred in a region that is, perhaps, more typical of major continental earthquakes. A right-lateral strike-slip earthquake rup-

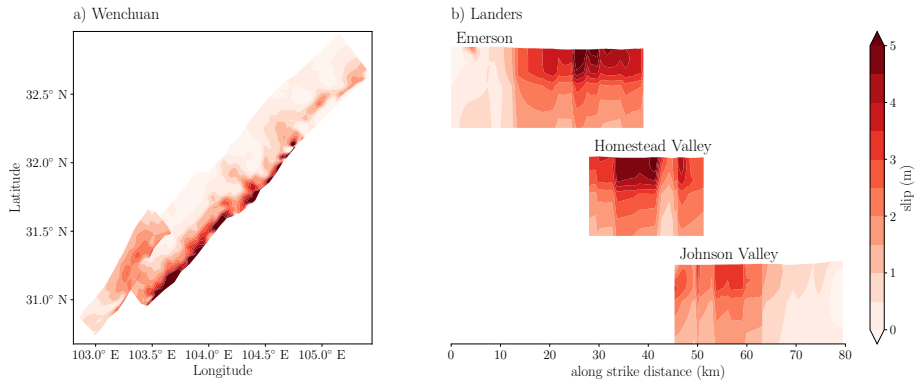


Figure 3: a) The magnitude of dip-slip in the Wenchuan earthquake inferred with our model including topography. b) The distribution of slip on the primary segments of the Landers rupture surface as inferred by our model including topographic effects. Note the lack of apparent shallow slip deficit. While the stepover segments are not included in this figure, our inversion does include those segments.

turing for 80 km, it involved failure across the Homestead Valley, Emerson, and Johnson Valley faults [3] in the Mojave desert, adjacent to a mix of flatter basins and steeper hilly or mountainous terrain. In addition, the large San Bernardino range is 25 km southwest with local relief of 2 to 3 km. We invert for the slip distribution on the fault model using the same methodology as for the Wenchuan earthquake with SRTM-based DEM data, the WGS-84 spheroid, and the fault model and GPS data from [3].

The slip distribution we infer is dominated by shallow right-lateral strike-slip on the southern Emerson, Homestead Valley and northern Johnson Valley segments (Figure 3). This general form of slip variation along strike is very similar to the along-strike variation found in [3]. Peak slip is located in the central Homestead Valley and central Emerson segments and reaches 5-7 meters, tapering off to the north and south. However, unlike [7], there is no apparent shallow slip deficit. In fact, there appears to be a shallow slip surplus. We quantify this in Figure 4 comparing the moment as a function of depth between our model and the vertical moment distribution in [9]. This difference suggests that, in the case of the Landers earthquake, the previously inferred shallow slip deficit was a modeling artifact due to neglecting topography.

The key difference in slip distribution between our model and the model of [9] is in the vertical distribution of moment. We find 101% higher moment in the shallowest km of the fault and 27% lower moment at 10 km depth. In the [9], 50% of the moment is located above 6.0 km depth, whereas in our model, 50% of the moment is located above 5.1 km depth. Essentially, the addition of topography “moves” moment from deep to shallow.

The fundamental issue here is that the least squares inversion process ampli-

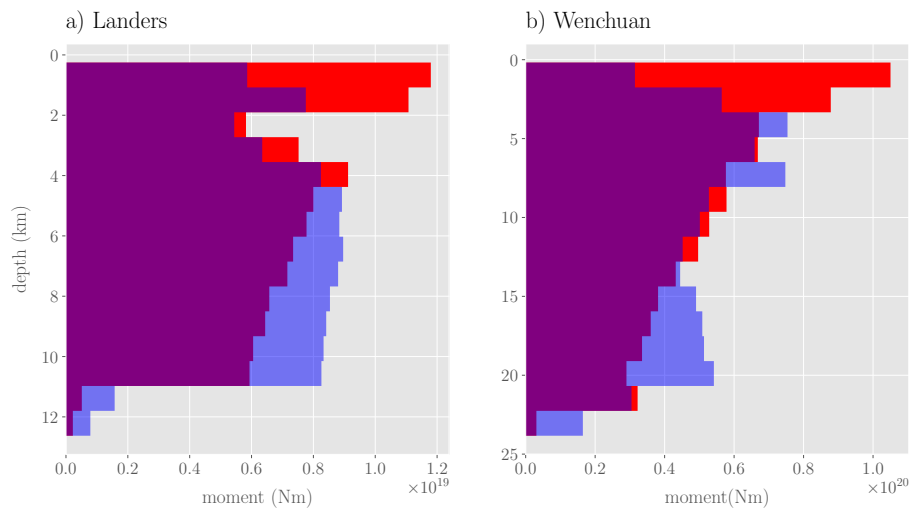


Figure 4: The distribution of moment with depth. a) The blue histogram shows the distribution of moment with depth inferred by [9] while the red histogram shows the moment distribution inferred by our model including topography. b) The blue histogram shows the distribution of moment with depth inferred by [20] while the red histogram shows the moment distribution inferred by our model including topography.

fies any physical model errors present in the forward model. Error amplification is linearly related to both the magnitude of the change in the forward model and the condition number of the regularized inverse problem[5]. In the inversions performed here, we saw condition numbers ranging from 5 to 100. Thus, the amplification of error from forward to inverse problem may be one or two orders of magnitude. This property of inversions suggests that more physically realistic models may be necessary for quantitatively accurate inference in earthquake science.

5 Conclusions

Moving towards more realistic fault models by including more accurate fault geometry, surface topography, and Earth curvature will enable improved understanding of the earthquake process. In the case of topography, we have shown that these improvements will be especially significant in the shallow portions of continental faults. For example, our work demonstrates that the magnitude of shallow slip may be systematically underestimated by widely used half-space models. In the case of the Wenchuan and Landers earthquakes, when topographic effects are included, we infer, respectively, 3 times and 2 times more shallow slip than previously reported. Beyond topography, the core issue here is that a small forward model error can be amplified by an order of magnitude in the inference of fault slip. This suggests that more physically accurate models are needed to determine the distribution of seismic rupture, aseismic creep and slow earthquakes. Such models will push forward our understanding of fault behaviors including the role of fluids, thermal properties and fault geometry.

6 Methods

6.1 Modern boundary element methods

We use Tectosaur, a new library for solving elastic boundary value problems based on the Symmetric Galerkin BEM [4]. Tectosaur combines linear interpolation over triangular elements with efficient fast multipole methods for far-field integrals and novel lookup-table-based numerical integration techniques for near-field integrals.

Previous BEM approaches have been based on analytical solutions for the displacement and stress induced by uniform slip on a triangular [2, 11] or rectangular surface [1]. These solutions suffer from a discontinuity in displacement at the boundary between elements, which results in unrealistic singular stress fields. By using a linear interpolation over each triangular element, Tectosaur is able to maintain slip and displacement continuity at element boundaries and avoid any singular stresses.

In addition, once a BEM problem is discretized and transformed into a linear system, analytical dislocation solutions suffer from a dense matrix that limits problem sizes to a few tens of thousands of elements. Instead, for the

far-field integrals, we use a simple Gaussian quadrature approach. Then, these integrals are efficiently approximated with the kernel-independent fast multipole method [8]. This results in a highly-accurate sparse approximation to the dense BEM matrix. As a result, Tectosaur can handle problems with many millions elements.

Deriving an analytical dislocation solution similar to [1] for triangular elements with linearly varying slip would be a monumental task. Instead, we use symmetry relations to design a small lookup table of all the possible near-field integrals. Then, we fill the lookup table using a brute-force limit-to-the-boundary numerical quadrature method. This is a numerical version of the symbolic algebra methods described in [13].

Tectosaur is implemented in Python and C++ with GPU acceleration available using both CUDA and OpenCL. Task-based parallelism techniques enable efficient use of many cores and multiple GPUs.

6.2 The role of physical model error in inverse problems

So far, we have discussed the influence of topographic model error on geodetic slip inversion. We have shown that the addition of topography on the order of 10-20% of the total fault depth leads to coseismic slip estimates that may be in error by almost 100%. This behavior should be expected since inversion processes amplify the error in the forward model.

A bound on the maximum error amplification can be related to the condition number of the inverse problem [5]. Consider a linear inverse problem:

$$\mathbf{G}m = d \tag{1}$$

where \mathbf{G} relates the unknown model parameters (e.g. slip distribution), m , to the known observations (e.g. surface displacements), d . If a small perturbation is applied to \mathbf{G} , $\Delta\mathbf{G}$, a classical result is that:

$$\frac{\|(\mathbf{G} + \Delta\mathbf{G})^{-1} - \mathbf{G}^{-1}\|}{\|\mathbf{G}^{-1}\|} \leq \kappa(\mathbf{G}) \frac{\|\Delta\mathbf{G}\|}{\|\mathbf{G}\|} \tag{2}$$

where for a matrix, \mathbf{X} , $\|\mathbf{X}\|$ denotes the largest singular value and $\kappa(\mathbf{G})$ is the condition number of \mathbf{G} .

That is to say, the inversion error amplification is linearly related to both the magnitude of the change in the forward model and the condition number of the regularized inverse problem. In the inversions performed here, we saw condition numbers ranging from 5 to 100. Thus, the amplification of error from forward to inverse problem may be one or two orders of magnitude. This property of inverse models suggests that more physically realistic models will be necessary for quantitatively accurate inference in earthquake science.

7 Acknowledgements

T. Ben Thompson appreciates the support of the Department of Energy Computational Science Graduate Fellowship.

8 Author Contributions

T.B.T performed the analysis and produced the figures. B.J.M. and T.B.T. interpreted the results and prepared the manuscript.

References

1. Okada, Y. Internal deformation due to shear and tensile faults in a half-space. *Bulletin of the Seismological Society of America* **82**, 1018–1040 (1992).
2. Thomas, A. L. *Poly3D: A three-dimensional, polygonal element, displacement discontinuity boundary element computer program with applications to fractures, faults, and cavities in the Earth's Crust* PhD thesis (Stanford University, 1993).
3. Hudnut, K. W. *et al.* Co-seismic displacements of the 1992 Landers earthquake sequence. *Bulletin of the Seismological Society of America* **84**, 625–645 (1994).
4. Bonnet, M., Maier, G. & Polizzotto, C. Symmetric Galerkin boundary element methods. *Applied Mechanics Reviews* **51**, 669–704 (1998).
5. El Ghaoui, L. Inversion error, condition number, and approximate inverses of uncertain matrices. *Linear algebra and its applications* **343**, 171–193 (2002).
6. Masterlark, T. Finite element model predictions of static deformation from dislocation sources in a subduction zone: sensitivities to homogeneous, isotropic, Poisson-solid, and half-space assumptions. *Journal of Geophysical Research: Solid Earth* **108** (2003).
7. Fialko, Y. Probing the mechanical properties of seismically active crust with space geodesy: Study of the coseismic deformation due to the 1992 Mw7.3 Landers (southern California) earthquake. *Journal of Geophysical Research: Solid Earth (1978-2012)* **109** (2004).
8. Ying, L., Biros, G. & Zorin, D. A kernel-independent adaptive fast multipole algorithm in two and three dimensions. *Journal of Computational Physics* **196**, 591–626 (2004).
9. Fialko, Y., Sandwell, D., Simons, M. & Rosen, P. Three-dimensional deformation caused by the Bam, Iran, earthquake and the origin of shallow slip deficit. *Nature* **435**, 295–299. ISSN: 0028-0836 (2005).

10. Vigny, C. *et al.* Insight into the 2004 Sumatra–Andaman earthquake from GPS measurements in southeast Asia. *Nature* **436**, 201 (2005).
11. Meade, B. J. Algorithms for the calculation of exact displacements, strains, and stresses for triangular dislocation elements in a uniform elastic half space. *Computers & Geosciences* **33**, 1064–1075. ISSN: 00983004 (Aug. 2007).
12. Masterlark, T. & Hughes, K. L. Next generation of deformation models for the 2004 M9 Sumatra-Andaman earthquake. *Geophysical Research Letters* **35** (2008).
13. Sutradhar, A., Paulino, G. H. & Gray, L. J. *Symmetric Galerkin Boundary Element Method* (Springer, 2008).
14. Shen, Z.-K. *et al.* Slip maxima at fault junctions and rupturing of barriers during the 2008 Wenchuan earthquake. *Nature geoscience* **2**, 718 (2009).
15. Thatcher, W. How the continents deform: The evidence from tectonic geodesy. *Annual Review of Earth and Planetary Sciences* **37**, 237–262 (2009).
16. Xu, X. *et al.* Coseismic reverse-and oblique-slip surface faulting generated by the 2008 Mw 7.9 Wenchuan earthquake, China. *Geology* **37**, 515–518 (2009).
17. Hubbard, J., Shaw, J. H. & Klinger, Y. Structural Setting of the 2008 Mw 7.9 Wenchuan, China, Earthquake. *Bulletin of the Seismological Society of America* **100**, 2713–2735 (2010).
18. Qi, W. *et al.* Rupture of deep faults in the 2008 Wenchuan earthquake and uplift of the Longmen Shan. *Nature Geoscience* **4**, 634 (2011).
19. Simons, M. *et al.* The 2011 magnitude 9.0 Tohoku-Oki earthquake: Mosaicking the megathrust from seconds to centuries. *science* **332**, 1421–1425 (2011).
20. Fielding, E. J. *et al.* Kinematic fault slip evolution source models of the 2008 M7. 9 Wenchuan earthquake in China from SAR interferometry, GPS and teleseismic analysis and implications for Longmen Shan tectonics. *Geophysical journal international* **194**, 1138–1166 (2013).
21. Meade, B. J., Klinger, Y. & Hetland, E. A. Inference of multiple earthquake-cycle relaxation timescales from irregular geodetic sampling of interseismic deformation. *Bulletin of the Seismological Society of America* **103**, 2824–2835 (2013).
22. Yokota, R. An FMM based on dual tree traversal for many-core architectures. *Journal of Algorithms & Computational Technology* **7**, 301–324 (2013).
23. Avouac, J.-P., Meng, L., Wei, S., Wang, T. & Ampuero, J.-P. Lower edge of locked Main Himalayan Thrust unzipped by the 2015 Gorkha earthquake. *Nature Geoscience* **8**, 708 (2015).

24. Xu, X. *et al.* Refining the shallow slip deficit. *Geophysical Journal International* **204**, 1867–1886 (2016).
25. *Loss and Damage Assessment after China Earthquake* <http://whc.unesco.org/en/news/439/>. Accessed: 2018-03-02.
26. *Mapzen, an open, sustainable, and accessible mapping platform.* <https://mapzen.com/>. Accessed: 2018-01-25.